

Diameter-Dependent Electron Mobility of InAs Nanowires

Alexandra C. Ford,^{†,‡,§,||} Johnny C. Ho,^{†,‡,§,||} Yu-Lun Chueh,^{†,‡,§,||} Yu-Chih Tseng,[‡] Zhiyong Fan,^{‡,§,||} Jing Guo,[‡] Jeffrey Bokor,^{‡,§} and Ali Javey^{*,‡,§,||}

Department of Electrical Engineering and Computer Sciences, University of California at Berkeley, Berkeley, California 94720, Materials Sciences Division, Lawrence Berkeley National Laboratory, Berkeley, California 94720, Berkeley Sensor and Actuator Center, University of California at Berkeley, Berkeley, California 94720, and Department of Electrical and Computer Engineering, University of Florida, Gainesville, Florida 32611

Received October 17, 2008; Revised Manuscript Received November 26, 2008

ABSTRACT

Temperature-dependent $I-V$ and $C-V$ spectroscopy of single InAs nanowire field-effect transistors were utilized to directly shed light on the intrinsic electron transport properties as a function of nanowire radius. From $C-V$ characterizations, the densities of thermally activated fixed charges and trap states on the surface of untreated (i.e., without any surface functionalization) nanowires are investigated while enabling the accurate measurement of the gate oxide capacitance, therefore leading to the direct assessment of the field-effect mobility for electrons. The field-effect mobility is found to monotonically decrease as the radius is reduced to <10 nm, with the low temperature transport data clearly highlighting the drastic impact of the surface roughness scattering on the mobility degradation for miniaturized nanowires. More generally, the approach presented here may serve as a versatile and powerful platform for in-depth characterization of nanoscale, electronic materials.

Semiconductor nanowires (NWs) have tremendous potential for applications in high-performance nanoelectronics and large-area flexible electronics.¹⁻⁹ In particular, InAs NWs are promising as the channel material for high-performance transistors because of their high electron mobility and ease of near-ohmic metal contact formation.¹⁰⁻¹⁴ Of particular interest is the dependence of the carrier mobility on NW radius for a given material, especially since smaller NWs are highly attractive for the channel material of nanoscale transistors as they enable improved electrostatics and lower leakage currents. Most theoretical studies have found carrier mobility to increase with radius for sub-10-nm Si NWs (no data available for InAs NWs), attributing the trend to either the dominant surface roughness scattering in smaller radius NWs¹⁵ or an enhanced phonon scattering rate due to an increased electron-phonon wave function overlap in smaller radius NWs.^{16,17} On the other hand, experimental reports in the literature have been contradictory, ranging from observation of mobility enhancement¹⁸ to degradation¹⁹ with Si

nanowire miniaturization for diameters (or widths) down to 10 nm. Therefore, the diameter dependency of the mobility highly depends on the specific nanowire material system,¹⁵⁻²⁰ the diameter range, and the method used to assess the electron mobility. The challenge in attaining accurate experimental data mainly arises from the difficulty of ohmic contact formation to nanoscale materials and the direct measurement of the gate capacitance. Here, we report the detailed current-voltage ($I-V$) and capacitance-voltage ($C-V$) spectroscopy of individual InAs NWs with ohmic contacts at different temperatures, therefore enabling the direct assessment of field-effect mobility as a function of NW diameter while elucidating the role of surface/interface fixed charges and trap states on the electrical properties.

InAs NWs used in this study were synthesized on Si/SiO₂ substrates by a physical vapor transport method using Ni nanoparticles as the catalyst as previous reported.²¹ The grown InAs NWs were over 10 μm long with a radius range of 7-20 nm (Figure 1a). The NWs are single crystalline with a native oxide thickness of 2-2.5 nm as evident from transmission electron microscopy (TEM) analysis (Figure 1, panels b and c). Importantly, the NWs grown using our previously reported conditions do not exhibit any noticeable tapering effect with a uniform diameter along the length of each NW, as confirmed by TEM and scanning electron microscopy (SEM). Energy dispersion spectrometry (EDS),

* Corresponding author, ajavey@eecs.berkeley.edu.

[†] These authors contributed equally.

[‡] Department of Electrical Engineering and Computer Sciences, University of California at Berkeley.

[§] Materials Sciences Division, Lawrence Berkeley National Laboratory.

^{||} Berkeley Sensor and Actuator Center, University of California at Berkeley.

[‡] Department of Electrical and Computer Engineering, University of Florida.

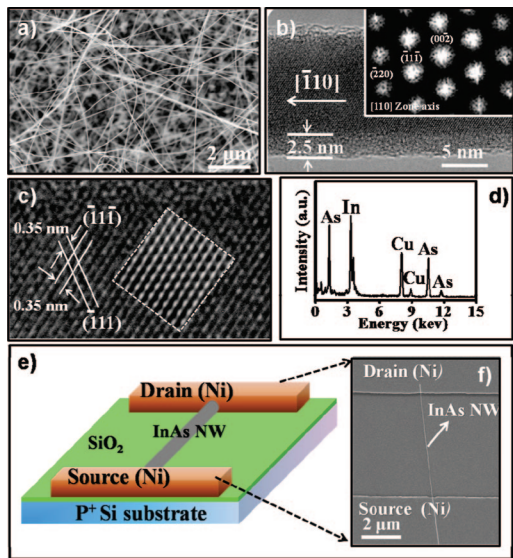


Figure 1. Electron microscopy characterization of InAs NWs. (a) SEM image of InAs NWs grown on a SiO₂/Si substrate by using Ni nanoparticles as the catalyst. (b) TEM image of a representative InAs NW. The inset shows the corresponding diffraction pattern converted by fast-Fourier transform where the zone axis of [110] can be identified. (c) The corresponding high-resolution TEM image taken from the NW in (b). (d) The EDS analysis shows that the chemical composition of In:As is close to 1:1. (e) A top-view schematic of a global back-gated NW FET, used for the I – V characterization. (f) SEM image of a representative back-gated NW FET.

as shown in Figure 1d, indicates that the chemical composition of In:As is close to 1:1.

For the electrical transport measurements, field-effect transistors in a back-gated configuration were fabricated (Figure 1, panels e–f, also see Supporting Information for fabrication details). Electrical properties of representative FETs with NW radius $r = 7.5$ – 17.5 nm are shown in Figure 2. Long channel lengths, $L = 6$ – 10 μm , were used for this study in order to ensure diffusive transport of carriers (rather than ballistic or quasi-ballistic transport), from which intrinsic transport properties, such as carrier mobility, can be deduced. Although the NWs were not intentionally doped, as expected, the devices exhibit an n-type behavior due to the high electron concentration of “intrinsic” InAs, arising from surface fixed charges and possible local imbalance in stoichiometry. Notably, for the channel lengths and NW diameters explored in this study, a linear dependence of the device resistance as a function of channel length is observed which is indicative of ohmic metal source/drain contacts (Ni) to InAs NWs.²² From the I – V characteristics (Figure 2, panels b–d), it is clearly evident that larger diameter NWs exhibit higher ON currents and more negative threshold voltages. Specifically, unit length normalized ON currents ($V_{\text{DS}} = 2$ V and $V_{\text{GS}} - V_{\text{t}} = 6$ V) of ~ 40 , 110, and 140 $\mu\text{A}-\mu\text{m}$ are obtained for $r = 7.5$, 12.5, and 17.5 nm NWs, respectively. This trend can be attributed to a larger cross-sectional area (i.e., effective channel width) for large diameter NWs but could also be indicative of reduced carrier scattering with increasing diameter. To further shed light on this trend, investigation of the electron transport properties as a function

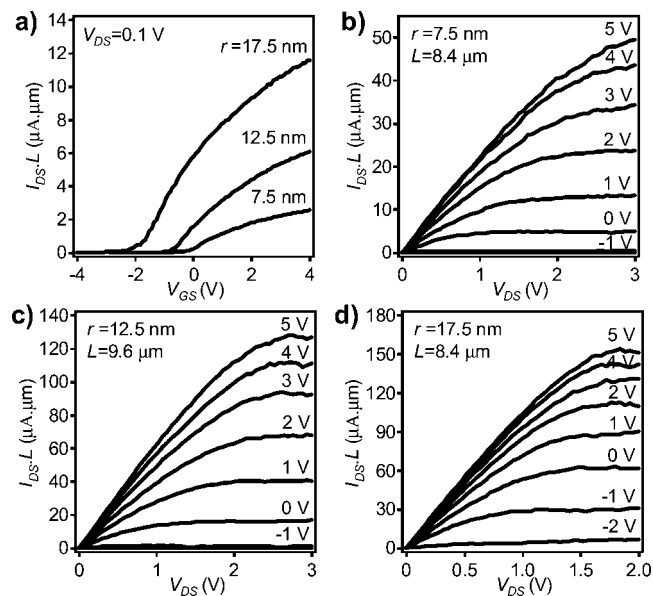


Figure 2. I – V characterization of InAs NW FETs. (a) Device output characteristics normalized for channel length ($I_{\text{DS}}L$ – V_{GS}) at $V_{\text{DS}} = 0.1$ V for three separate long channel devices ($L = 8.4$, 9.6 , and 8.4 μm , respectively) with NW radii of $r = 17.5$, 12.5 , and 7.5 nm, respectively. The 2.5 nm oxide shell was subtracted from the measured NW radius. Length normalized $I_{\text{DS}}L$ – V_{DS} plots for various V_{GS} for the (b) 7.5 nm, (c) 12.5 nm, and (d) 17.5 nm radius NW devices. The NW diameter for each device was directly obtained from the atomic force microscopy and SEM analyses, with an uncertainty of $\sim \pm 1$ nm. All measurements were conducted in a vacuum ambient with minimal hysteresis.²¹

of NW radius is imperative. Particularly, electron mobility, μ_{n} , is an important figure of merit as it relates the drift velocity of electrons to an applied electric field. Accurate and direct measurement of the gate oxide capacitance, however, is needed for the extraction of field-effect mobility from I – V characteristics.

In order to determine the gate oxide capacitance of NW FETs and to shed light on the density and characteristics of the surface/interface trap states and fixed charges, direct C – V measurements were performed on *single*-InAs NW devices at various temperatures. Previously, the only reported C – V measurements for InAs NW FETs have been for parallel arrays of NWs (> 100 vertical NWs per device) and at room temperature.²³ For the purpose of this work, temperature-dependent C – V spectroscopy of *single*-NW devices with known NW radius are required to minimize the averaging effects and shed light on properties of individual NWs. Hence, we utilized a method previously developed by Ilani et al. in order to measure the small capacitance signal (10 aF to 1 fF) of *single*-NW FETs over a large background parasitic capacitance (~ 30 fF).^{24,25} A similar method was also utilized in the past by Tu, R., et al. to examine the gate oxide capacitance of single Ge NW FETs.²⁵ As depicted in Figure 3a, buried-gate InAs NW FETs with $t_{\text{ox}} \sim 60$ nm, S/D length $L_{\text{SD}} \sim 10$ μm , and buried-gate length $L_{\text{LG}} \sim 5$ μm were fabricated. Details of the C – V measurement setup and device fabrication can be found in the Supporting Information.

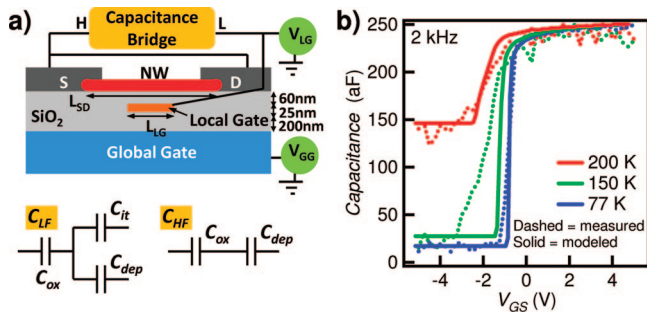


Figure 3. $C-V$ characterizations of InAs NW FETs. (a) Measurement schematics for $C-V$ measurement of a single NW device (top) and the equivalent capacitance circuits in the depletion regime for low-frequency (LF) and high-frequency (HF) measurements (bottom). H and L represent the “high” and “low” terminals of the bridge, respectively. (b) Temperature-dependent $C-V$ characteristics for a local-gated NW FET with $r \sim 11$ nm and $L_{LG} \sim 4.7$ μm . Electrostatic modeling is also applied and fitted to all measurements for the normalized gate capacitance.

Figure 3b shows the temperature dependency of $C-V$ characteristics for a representative InAs NW FET ($r \sim 11$ nm, $L_G = 4.7$ μm , $L_{SD} = 9.3$ μm) obtained with an AC signal of 125 mV at 2 kHz. For this device, a flat-band voltage of $V_{FB} \sim 0$ V (corresponding to the on-set voltage of the sharp decrease in the measured capacitance) is observed, with $V_{LG} > V_{FB} \sim 0$ V resulting in the accumulation of electrons in the n-type InAs channel (i.e., ON state). We note that this is in distinct contrast to the operation mode of the conventional MOSFETs in which the ON state corresponds to the inversion of the channel (rather than accumulation). The gate capacitance value obtained in the accumulation regime corresponds to the oxide capacitance, $C_{LG,accumulation} = C_{ox}$, which is temperature independent. When $V_{LG} < V_{FB}$ (i.e., $V_{LG} < 0$ V), the channel is depleted of electrons, thus resulting in the reduction of the total gate capacitance due to the addition of the semiconductor capacitance, C_s , in series with C_{ox} (i.e., $C_{LG,depletion} = C_{ox} C_s / (C_{ox} + C_s)$). At this state, the NW channel is effectively turned “OFF”. The temperature-dependent $C-V$ measurements illustrate two important effects (Figure 3b). First, a shift in V_{FB} is observed as a function of temperature which can be attributed to the change in the population density of the thermally activated, donor-like fixed charges, N_s (near the conduction band edge, in the unit of cm^{-2}), at the NW surface/interface. Second, the capacitance in the depletion region is drastically reduced as the temperature is lowered from 200 to 150 K but relatively unchanged thereafter. This trend is a clear signature of thermally activated, surface/interface traps (with density, D_{it}) as they induce a capacitance, C_{it} , in parallel to C_s (Figure 3a); therefore, effectively increasing $C_{LG,depletion}$. For this case, the gate capacitance in the depletion regime is given as, $C_{LG,depletion} = C_{ox} (C_s + C_{it}) / (C_{ox} + C_s + C_{it})$. Below 150 K, the measured depletion capacitance is independent of temperature, indicating that the traps stop responding. On the basis of this analysis, we extrapolate $C_s \sim 10.5$ aF and $C_{it} \sim 0, 11.3,$ and 316 aF at 77, 150, and 200 K, respectively. Similar C_{it} values with $D_{it} \sim 2 \times 10^{11}$ states cm^{-2} eV $^{-1}$ at 200 K were obtained from frequency-dependent measurements (2 and 20 kHz, see Supporting Information, Figures

S1 and S2). It is important to note that 2 kHz may not present the true low frequency operation regime as some traps may already be irresponsive at that frequency. Therefore, the extracted D_{it} values only represent a lower bound limit. We were not able to perform $C-V$ measurements at temperatures higher than 200 K due to the thermal noise and leakage currents of low band gap ($E_g \sim 0.36$ eV) InAs NW channels (arising from the band-to-band thermal generation of carriers).

Detailed electrostatic modeling was also performed to further investigate the effect of fixed charges and trap states on the $C-V$ characteristics. A two-dimensional Poisson equation was self-consistently solved with the equilibrium carrier statistics for the InAs NW and the native oxide layer for a cross section perpendicular to the nanowire axis. Both N_s and D_{it} are treated as the fitting parameters in the simulation. A close fit of the experimental data for the normalized gate capacitance, as shown in Figure 3b, is obtained when assuming $N_s = 0, 1.5 \times 10^{11},$ and 4.5×10^{11} states cm^{-2} and $C_{it} = 0, 17.4,$ and 344 aF for 77, 150, and 200 K, respectively, which is consistent with the values extrapolated from the analytical expressions described above. When quantum effects²³ are taken into consideration by self-consistently solving the Poisson and Schrödinger equations in the quantum simulation, it is found that quantum effects decrease the semiconductor capacitance by shifting the centroid of the charge away from the NW surface. However, because in our fabricated FETs the gate oxide thickness is much larger than the NW radius (~ 3 to 7 times larger), the quantum effects on the total gate capacitance are relatively small (Supporting Information, Figure S4).²⁶

In addition to the detailed characterization of C_{it} and D_{it} , we were able to directly measure C_{ox} as a function of NW radius. Figure 4 shows the experimentally obtained C_{ox} for different NW FETs with $r = 10-20$ nm. We also performed electrostatic modeling of the oxide capacitance values by using the finite element analysis software package Finite Element Method Magnetics (Figure 4). The measured and modeled capacitance values are in qualitative agreement, with the experimental values $\sim 25\%$ higher than the modeled results. We attribute this discrepancy to the infringing capacitances between LG and the overlapped NW segments which were ignored in the simulation as well as the geometric

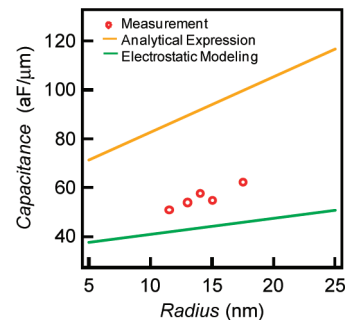


Figure 4. Measured and simulated gate oxide capacitance as a function of radius per unit of local buried gate length. For the simulation, a semiconductor nanowire with $\epsilon = 15$ was assumed. Additionally, the capacitance values obtained from the analytical expression of eq 1 are shown.

uncertainties associated with the fabricated NW FETs (i.e., the exact thickness of the gate oxide deposited on Pt LGs). Additionally, C_{ox} was calculated from the analytical expression

$$C_{\text{ox}} = \frac{2\pi\epsilon\epsilon_0L}{\cosh^{-1}[(r+t_{\text{ox}})/r]} \quad (1)$$

which corresponds to the capacitance of a cylindrical wire on a planar substrate and is often used in the literature for NW device analysis.^{26–30} Here, ϵ is the dielectric constant of the gate insulator ($\epsilon = 3.9$ for SiO_2) and ϵ_0 is the permittivity of free space. The capacitance values obtained from this analytical expression are $\sim 2\times$ higher than the experimental values (Figure 4), demonstrating the lack of accuracy of this analytical method for NW FET performance analyses.

We next assess the field-effect electron mobility of InAs NW FETs by using the low-bias ($V_{\text{DS}} = 0.1$ V) transconductance

$$g_{\text{m}} = \left. \frac{dI_{\text{DS}}}{dV_{\text{GS}}} \right|_{V_{\text{DS}}}$$

and the analytical expression

$$\mu_{\text{n}} = g_{\text{m}} \frac{L^2}{C_{\text{ox}} V_{\text{DS}}}$$

Figure 5a shows μ_{n} as a function of V_{GS} for three different NW radii, corresponding to the $I_{\text{DS}}-V_{\text{GS}}$ plot of Figure 2a. It is clearly evident that the peak field-effect mobility is enhanced for larger diameter NWs with $\mu_{\text{n}} \sim 2500, 4000,$ and $6000 \text{ cm}^2/(\text{V}\cdot\text{s})$ for $r \sim 7.5, 12.5,$ and 17.5 nm, respectively. Notably, the $\mu_{\text{n}}-V_{\text{GS}}$ characteristics for all measured NW FETs exhibit a near identical behavior with the field-effect mobility at first increasing with $V_{\text{GS}}-V_{\text{t}}$ before sharply decaying at high electric fields. This decay can be attributed to the enhanced surface scattering of the electrons at high gate fields, similar to the behavior that is observed in conventional Si MOSFETs. In addition, in quasi 1-dimensional (1-D) NWs, due to the quantization of sub-bands, the metal contacts may not enable a sufficient injection of electrons into the channel at high electric fields as desired

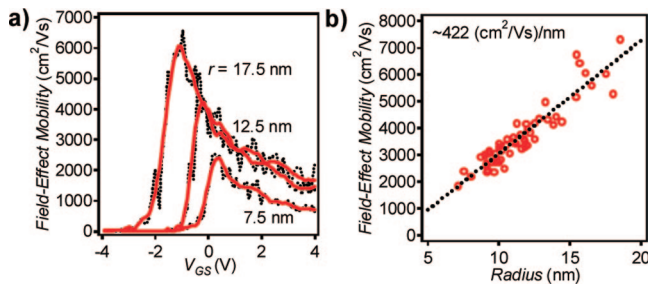


Figure 5. Room temperature mobility assessment. (a) Field-effect mobility as a function of V_{GS} for three NWs of different radii ($r = 17.5, 12.5,$ and 7.5 nm), corresponding to the $I_{\text{DS}}L-V_{\text{GS}}$ plot of Figure 2a. (b) Peak field-effect mobility as a function of radius for more than 50 different devices with NWs ranging from 7–18 nm in radius post oxide subtraction. Over this NW radius range, the peak field-effect mobility linearly increases with radius, closely fitting the linear expression $\mu_{\text{n}} = 422r - 1180$. Note that the $I_{\text{DS}}-V_{\text{GS}}$ plots were smoothed before the transconductance, g_{m} was calculated for field-effect mobility assessment.

by the gate potential. Because of the finite sub-band energy spacing, Schottky barriers to the higher sub-bands are often formed at the NW–metal contact interfaces, therefore lowering the transconductance and the mobility of the FETs at high gate voltages. While at a first glance, the NWs used in this study may seem rather large to exhibit quantization effects, due to the large Bohr radius of InAs (~ 34 nm),¹³ even a $r = 10$ nm NW can be treated as quasi-1-D because the confinement energies for the lowest and second lowest sub-bands are ~ 100 and 240 meV, respectively (Supporting Information, Figure S3).³¹ Figure 5b illustrates the peak field-effect mobility as a function of InAs NW radius for more than 50 different FETs with $r = 7-18$ nm. Over this NW radius range, the peak mobility linearly increases with radius with a slope of $\sim 422 \text{ (cm}^2/(\text{V}\cdot\text{s}))/\text{nm}$. We note that larger or smaller radii beyond the range reported here were not explored due to the difficulty with their growth using our condition.²¹ The linear drop in the field-effect mobility with reduced NW radius may be attributed to a number of factors, including the enhanced phonon–electron wave function overlap (i.e., enhanced phonon scattering of electrons), the increased surface scattering, enhanced defect scattering, and the lower effective gate coupling factor due to the surface states (D_{it})¹¹ for miniaturized NWs with high surface area to volume ratio. Additionally, at a first glance, a diameter-dependent contact resistance may be expected which could also affect the extracted field-effect mobility.³² However, that appears not to be the case since for the diameter and length regime explored in this study, we find a linear dependence of the ON-state resistance as a function of the channel length.²² Therefore, the main source of the total device resistance is due to the channel resistance.

It should be noted that the electron mobility reported in this work is the so-called “field-effect” mobility, distinct from the effective mobility and the Hall mobility. The Hall mobility represents the bulk carrier transport with no major contributions from the surface and quantization effects while both the field-effect and effective mobilities are used to characterize the carrier transport in the surface inversion (or accumulation, in the case of InAs NWs) layer of the MOSFETs. The field-effect and effective mobilities are, however, deduced from the $I-V$ characteristics by using different analytical models. Specifically, the effective mobility is deduced from the drain conductance

$$g_{\text{D}} = \left. \frac{dI_{\text{DS}}}{dV_{\text{DS}}} \right|_{V_{\text{GS}}}$$

with

$$\mu_{\text{n,eff}} = g_{\text{D}} \frac{L^2}{C_{\text{ox}} (V_{\text{GS}} - V_{\text{t}})}$$

On the other hand, as described above, the field-effect mobility is deduced from the transconductance, g_{m} . Therefore, the main difference between the field-effect and effective mobility is the neglect of the gate electric-field dependence in the field-effect mobility expression.³³ For the device modeling, effective mobility is often used to predict the current and switching speeds. A difficulty in the accurate assessment of the effective mobility arises from the error associated with finding V_{t} from the measured $I-V$ characteristics. Therefore, for the purpose of this work, we focus on the presentation of the field-effect mobility which presents

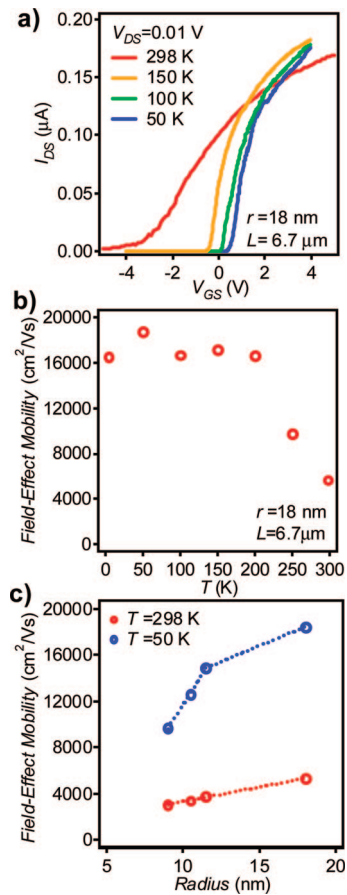


Figure 6. Temperature-dependent electron transport properties. (a) $I_{DS}-V_{GS}$ at $V_{DS} = 0.01$ V for a representative NW FET with $r = 18$ nm and $L = 6.7 \mu\text{m}$ over a temperature range of 50–298 K. (b) The corresponding peak field-effect mobility as a function of temperature for the same device. (c) The dependency of field-effect mobility on radius for four NWs of different radii at temperatures of 50 and 298 K.

the lower bound value of the true electron mobility in InAs NWs (field-effect mobility is lower than the effective mobility, except for low gate fields). However, even if the effective mobility analysis is used, a similar diameter dependency for the peak mobility is observed for InAs NWs as depicted in Figure S5 of the Supporting Information.

In an effort to shed light on the source of mobility degradation for smaller NWs, temperature-dependent electron transport measurements were conducted. Typical $I_{DS}-V_{GS}$ plots at $V_{DS} = 0.01$ V for a back-gated NW device with $r = 18$ nm and $L = 6.7 \mu\text{m}$ are shown in Figure 6a over a temperature range of 50–298 K. Figure 6b shows the corresponding peak field-effect mobility as a function of temperature for this device, showing a linear enhancement of the peak electron field-effect mobility from ~ 6000 to $16000 \text{ cm}^2/(\text{V}\cdot\text{s})$ as the temperature is reduced from 298 to 200 K. Below ~ 200 K, minimal change in the field-effect mobility is observed. We attribute this to the transition temperature at which the surface roughness scattering becomes dominant over other scattering events caused by acoustic phonon and/or surface/interface trap states. Additionally, at lower temperatures, since the surface trap states are fully frozen, they should not have an impact on the gate coupling factor. The dependency of field-effect mobility on

the NW radius was also investigated at different temperatures and the data for four NW FETs with $r = 8-20$ nm at 298 and 50 K are shown in Figure 6c. Even at low temperatures (i.e., 50 K), in the regime where phonons and surface/interface traps are frozen out, the monotonic increase of mobility with radius is clearly evident. Specifically, at 50 K, a near-linear trend is observed for small radius NWs (i.e., $r \leq 12$ nm, slope of $\sim 2077 \text{ (cm}^2/(\text{V}\cdot\text{s}))/\text{nm}$ with the field-effect mobility approaching a saturation value of $\sim 18000 \text{ cm}^2/(\text{V}\cdot\text{s})$ for larger NWs (i.e., $r > 18$ nm). The phonon population is drastically reduced at 50 K, and therefore, the acoustic phonon scattering for low-field transport can be assumed to be nonexistent. Additionally, most surface/interface traps are frozen out at such low temperatures and should not affect the gate electrostatic coupling or the electron transport properties near the surface. Impurity scattering should not be a factor since the NWs are not intentionally doped. As a result, the observed dependency of electron field-effect mobility on NW radius at 50 K is mainly attributed to the enhanced surface roughness scattering of electrons in the miniaturized NWs. As the NW radius is reduced, electron transport near the surface dominates the electrical characteristics. However, the atomic roughness of the surface results in an enhanced carrier scattering, therefore effectively lowering the carrier mobility. Specifically, the surface roughness scattering rate depends on the surface-area to volume ratio; therefore, a near linear dependency of μ_n on radius for smaller diameter NWs is expected. Since surface roughness scattering is nearly independent of temperature, the difference between the observed trends at 50 and 298 K arise from a combination of phonon scattering and surface/interface traps and fixed charges that contribute to additional surface scattering and lower gate coupling.

Future theoretical analysis of the various scattering events discussed above is needed to enable more detailed and quantitative understanding of the role of each scattering mechanism for a given NW radius and temperature range. Additionally, the electron effective mass may increase with the diameter miniaturization which could also have an impact in the diameter dependency of the mobility and requires future theoretical insights. Clearly, the results presented here demonstrate the drastic effect of NW radius on the field-effect mobility. This is of concern since small diameter NWs ($r < \sim 10$ nm) are highly desirable for the channel material of future sub-10-nm FETs as they enable improved gate electrostatic control of the channel and lower leakage currents. However, this work suggests that the aggressive diameter scaling of NWs may only be attained at the cost of field-effect mobility degradation, therefore requiring careful device design considerations for achieving the optimal device performances. Additionally, improving the surface properties is essential for enhancing the electron transport characteristics and the electrostatics of InAs NW FETs.^{10,12} A similar approach of utilizing $C-V$ and $I-V$ characterizations may be used in the future to systematically study the precise role of surface functionalization or high- κ gate dielectric integration on the electrical properties of InAs NW FETs.

In summary, an approach for in-depth characterization of the intrinsic electronic properties of nanoscale materials is presented by utilizing detailed $C-V$ and $I-V$ measurements. Specifically, the $C-V$ behavior of single InAs NW FETs was successfully characterized for different temperatures and measuring frequencies. From the $C-V$ measurements, information regarding C_{ox} , C_{it} , and D_{it} was directly acquired while enabling the accurate assessment of field-effect mobility. The room temperature, field-effect mobility is found to linearly increase with radius for $r = 7-18$ nm. The dependency of mobility on radius at low temperature (i.e., 50 K) where the phonons and interface traps are thermally frozen out sheds light on the enhanced role of surface transport and surface scattering in smaller NWs. In the future, this approach can be utilized to systematically study the effects of surface passivation on the field-effect mobility and surface/interface traps and fixed charges.

Acknowledgment. This work was supported by Intel Corporation, MARCO/MSD Focus Center Research Program, and Berkeley Sensor and Actuator Center. J.C.H. acknowledges an Intel Graduate Fellowship. The synthesis part of this work was supported by a LDRD from Lawrence Berkeley National Laboratory. All fabrication was performed at the UC Berkeley Microlab facility. We thank Z. A. Jacobson for help with fabrication.

Supporting Information Available: NW FET fabrication details, $C-V$ measurement setup, frequency-dependent $C-V$ characterization, effective mobility, and the effect of quantum capacitance on the total gate capacitance. This material is available free of charge via the Internet at <http://pubs.acs.org>.

References

- (1) Lieber, C. M.; Wang, Z. L. *MRS Bull.* **2007**, *32*, 99–104.
- (2) Javey, A. *ACS Nano* **2008**, *2*, 1329–1335.
- (3) Bryllert, T.; Wernersson, L. E.; Froberg, L. E.; Samuelson, L. *IEEE Electron Device Lett.* **2006**, *27*, 323–325.
- (4) Friedman, R. S.; McAlpine, M. C.; Ricketts, D. S.; Ham, D.; Lieber, C. M. *Nature* **2005**, *434*, 1085.
- (5) Fan, Z.; Ho, J. C.; Jacobson, Z. A.; Razavi, H.; Javey, A. *Proc. Natl. Acad. Sci. U.S.A.* **2008**, *105*, 11066–11070.
- (6) Fan, Z.; Ho, J. C.; Jacobson, Z. A.; Yerushalmi, R.; Alley, R. L.; Razavi, H.; Javey, A. *Nano Lett.* **2008**, *8*, 20–25.
- (7) Wang, X. D.; Song, J. H.; Liu, J.; Wang, Z. L. *Science* **2007**, *316*, 102–105.
- (8) Xiang, J.; Lu, W.; Hu, Y. J.; Wu, Y.; Yan, H.; Lieber, C. M. *Nature* **2006**, *441*, 489–493.
- (9) McAlpine, M. C.; Ahmad, H.; Wang, D.; Heath, J. R. *Nat. Mater.* **2007**, *6*, 379–384.
- (10) Jiang, X.; Xiong, Q.; Nam, S.; Qian, F.; Li, Y.; Lieber, C. M. *Nano Lett.* **2007**, *7*, 3214–3218.
- (11) Dayeh, S.; Soci, S.; Yu, P.; Yu, E.; Wang, D. *Appl. Phys. Lett.* **2007**, *90*, 162112-1-3.
- (12) Hang, Q.; Wang, F.; Carpenter, P. D.; Zemlyanov, D.; Zakharov, D.; Stach, E. A.; Buhro, W. E.; Janes, D. B. *Nano Lett.* **2008**, *8*, 49–55.
- (13) Lind, E.; Persson, A. I.; Samuelson, L.; Wernersson, L. E. *Nano Lett.* **2006**, *6*, 1842–1846.
- (14) Bleszynski, A. C.; Zwanenburg, F. A.; Westervelt, R. M.; Roest, A. L.; Bakkers, E. P. A. M.; Kouwenhoven, L. P. *Nano Lett.* **2007**, *7*, 2559–2562.
- (15) Lenzi, M.; Gnudi, A.; Reggiani, S.; Gnani, E.; Rudan, M.; Baccarani, G. *J. Comput. Electron.* **2008**, *7*, 355–358.
- (16) Kotlyar, R.; Obradovic, B.; Matagne, P.; Stettler, M.; Giles, M. D. *Appl. Phys. Lett.* **2004**, *84*, 5270–5272.
- (17) Ramayya, E. B.; Vasileska, D.; Goodnick, S. M.; Knezevic, I. *IEEE Trans. Nanotechnol.* **2007**, *6*, 113–117.
- (18) Koo, S.-M.; Fujiwara, A.; Han, J.-P.; Vogel, E. M.; Richter, C. A.; Bonevich, J. E. *Nano Lett.* **2004**, *4*, 2197–2201.
- (19) Chen, J.; Saraya, T.; Miyaji, K.; Shimizu, K.; Hiramoto, T. *Symp. VLSI Technol.* **2008**, 32–33.
- (20) Motayed, A.; Vaudin, M.; Davydov, A. V.; MeIngailis, J.; He, M.; Mohammad, S. N. *Appl. Phys. Lett.* **2007**, *90*, 043104.
- (21) Ford, A. C.; Ho, J. C.; Fan, Z.; Ergen, O.; Altoe, V.; Aloni, S.; Razavi, H.; Javey, A. *Nano Res.* **2008**, *1*, 32–39.
- (22) Chueh, Y.-L.; Ford, A. C.; Ho, J. C.; Jacobson, Z. A.; Fan, Z.; Chen, C.-Y.; Chou, L.-J.; Javey, A. *Nano Lett.* **2008**, *8*, 4528–4533.
- (23) Karlström, O.; Wacker, A.; Nilsson, K.; Astromskas, G.; Roddaro, S.; Samuelson, L.; Wernersson, L. E. *Nanotechnology* **2008**, *19*, 435201.
- (24) Ilani, S.; Donev, L. A. K.; Kindermann, M.; McEuen, P. L. *Nat. Phys.* **2006**, *2*, 687–691.
- (25) Tu, R.; Zhang, L.; Nishi, Y.; Dai, H. *Nano Lett.* **2007**, *7*, 1561–1565.
- (26) Javey, A.; Kim, H.; Brink, M.; Wang, Q.; Ural, A.; Guo, J.; McIntyre, P.; McEuen, P.; Lundstrom, M.; Dai, H. *Nat. Mater.* **2002**, *1*, 241–246.
- (27) Wang, D.; Wang, Q.; Javey, A.; Tu, R.; Dai, H.; Kim, H.; Krishnamohan, T.; McIntyre, P.; Saraswat, K. *Appl. Phys. Lett.* **2003**, *83*, 2432–2434.
- (28) Duan, X.; Huang, Y.; Cui, Y.; Wang, J.; Lieber, C. M. *Nature* **2001**, *409*, 66–69.
- (29) Huang, Y.; Duan, X.; Cui, Y.; Lieber, C. M. *Nano Lett.* **2002**, *2*, 101–104.
- (30) Bryllert, T.; Samuelson, L.; Jensen, L.; Wernersson, L. *DRC Proc.* **2005**, *1*, 157.
- (31) Guo, J. Unpublished, 2008.
- (32) Leonard, F.; Talin, A. *Phys. Rev. Lett.* **2006**, *97*, 026804–1–4.
- (33) Arora, N. *MOSFET Modeling for VLSI Simulation*; World Scientific: Singapore, 2006.

NL803154M

Supporting Information

Diameter-Dependent Electron Mobility of InAs Nanowires

Alexandra C. Ford^{1,2,3,†}, Johnny C. Ho^{1,2,3,†}, Yu-Lun Chueh^{1,2,3,†}, Yu-Chih Tseng¹, Zhiyong Fan^{1,2,3}, Jing Guo⁴, Jeffrey Bokor^{1,2}, Ali Javey^{1,2,3,*}

¹Department of Electrical Engineering and Computer Sciences, University of California at Berkeley, Berkeley, CA, 94720, USA.

²Materials Sciences Division, Lawrence Berkeley National Laboratory, Berkeley, CA 94720, USA.

³Berkeley Sensor and Actuator Center, University of California at Berkeley, Berkeley, CA, 94720, USA.

⁴Department of Electrical and Computer Engineering, University of Florida, Gainesville, Florida 32611

[†] These authors contributed equally.

* Corresponding author: ajavey@eecs.berkeley.edu

Device Fabrication for I-V Measurements:

First, InAs NWs were harvested in an ethanol solution by a gentle sonication process, and drop-casted on a p⁺Si/SiO₂ (~53 nm, thermally grown) substrate. Metal source/drain (S/D) contacts were then defined by photolithography, Ni evaporation (~50 nm thick), and lift-off. In this configuration, the p⁺Si substrate serves as the global back-gate with a gate dielectric thickness of $t_{ox} \sim 53$ nm SiO₂. To ensure an ohmic contact formation, a 5sec HF etch (~0.1%) was applied immediately prior to the Ni contact evaporation to remove the native oxide on the exposed NW surfaces. Additionally, the fabricated devices were annealed at 250°C for 1min to further improve the contact properties.

Device Fabrication for C-V Measurements:

First, ~225nm thick SiO₂ was grown on top of a p⁺Si substrate by wet oxidation at 1000°C for 27 min 30 sec. The local gates were then defined by photolithography patterning of the resist, 60 sec 10:1 HF etch, DI water rinse, Ti/Pt evaporation (~ 1 nm / 24 nm thick), and lift-off. The oxide etching and metal evaporation steps were well calibrated and controlled to ensure the flatness of the local gate fingers with the nearby oxide regions. After this, 60 nm thick low-temperature oxide (LTO) was grown by LPCVD at 400°C for 4 min 30 sec and annealed at 700°C in forming gas for 5 min. InAs NWs were then drop-casted onto the sample. Metal source/drain (S/D) contacts were defined by photolithography, Ni evaporation (~50 nm thick), and lift-off. A 5sec HF etch (~0.1%) was applied immediately prior to the Ni evaporation to remove the native oxide in the control regions. Finally, the fabricated devices were annealed at 250°C for 1 min to further enhance the contact properties.

C-V measurement set-up

The relatively long ($\sim 2.5 \mu\text{m}$) underlapped region on each side of the local-gate (LG) reduces the parasitic capacitance between LG and S/D, therefore, enabling the direct measurement of the NW/LG capacitance. The two underlapped NW segments effectively work as nanoscale “contacts” to the NW channel with their conduction being modulated by the global back-gate (GG, i.e., p^+Si substrate) potential. The capacitance measurements were carried out with a capacitance bridge (Andeen-Hagerling, model 2700A) in a variable temperature cryogenic probe station (Lakeshore, model TTPX). During the C - V measurements, S/D electrodes were electrostatically grounded, and a constant bias of $V_{GG}=2\text{V}$ was applied to the GG to turn ON the underlapped regions while the charge in the NW channel was modulated by the LG voltage, V_{LG} . The background capacitance was measured by applying a negative bias to the GG, $V_{GG}=-5\text{V}$, in order to turn OFF the underlapped NW segments, therefore enabling the accurate extraction of the capacitance, C_{LG} as a function of V_{LG} .

Frequency-dependent C-V measurements

Beside C - V measurements at 2kHz, we performed measurements at a higher frequency of 20kHz in order to further shed light on the nature of surface/interface traps. At high frequencies, it is expected that the traps would not have enough time to charge and/or discharge, therefore, not affecting the measured C - V characteristics.

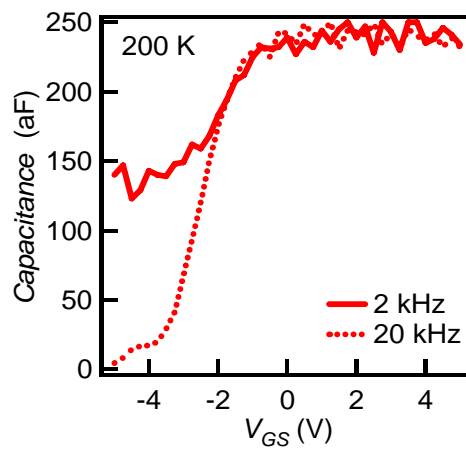


Figure S1. C - V characteristics for two different measurement frequencies (2kHz and 20kHz) at 200K. This data is for the same device as that of Fig. 3.

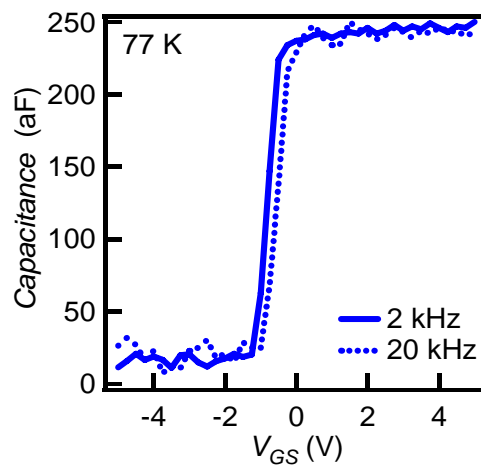


Figure S2. C - V characteristics for two different measurement frequencies (2kHz and 20kHz) at 77K for the same NW device shown in Fig. S1 and Fig. 3.

Figures S1 and S2 demonstrate the frequency dependence of C - V for the same NW FET at 200K and 77K, respectively. At 200K, similar capacitance values are obtained in the accumulation regime for both high (HF) and low frequency (LF) measurements. This is expected since C_{ox} does not exhibit any dependence on the operation frequency. However, the depletion regime exhibits a drastic frequency-dependent response. The frequency dependent response of the capacitance in the depletion region is attributed to C_{it} with a density of surface/interface traps

of $D_{it} = \frac{C_{LF} - C_{HF}}{q \left(1 - \frac{C_{LF}}{C_{ox}}\right) \left(1 - \frac{C_{HF}}{C_{ox}}\right) 2\pi\omega L_{LG}}$, where C_{LF} and C_{HF} are the low and high frequency gate

capacitances, respectively.¹ From this analysis, we extract $C_{it} \sim 335 \text{ aF}$ and $D_{it} \sim 2 \times 10^{11} \text{ states cm}^{-2} \text{ eV}^{-1}$ at 200K, both of which are consistent with those obtained from the temperature dependent analysis described above. At 77K, there is no obvious difference between the HF and LF C - V characteristics in the accumulation or depletion regimes, suggesting that the majority of traps are thermally frozen. The maximum and minimum frequencies of 20kHz and 2kHz used in this study were the limits of our instrumentation set up, as at lower frequencies, inadequate signal to noise was attained while the capacitance bridge was limited to 20kHz in operation.

Computed InAs NW Density of States

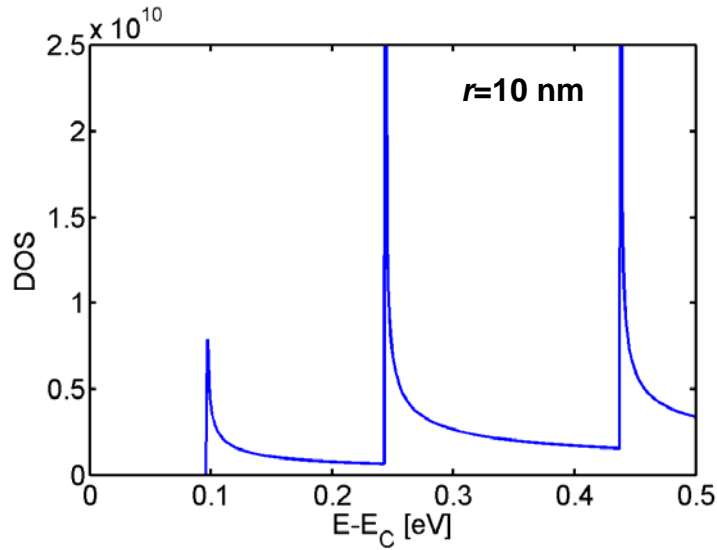


Figure S3. The computed density-of-states (DOS) for a cylindrical InAs nanowire with a radius of 10nm. An electron effective mass of $0.023m_0$ was used. A two-dimensional Schrodinger equation was solved for the cylindrical cross section of the nanowire to obtain the subbands, and the density-of-states is subsequently computed by the summation of the DOS over all subbands. Electron wave penetration from the InAs nanowire to the oxide is neglected. The result shows that the subband spacing is larger than the room temperature thermal energy even for a NW diameter of 20nm.

Semiconductor Capacitance by semiclassical and quantum simulations

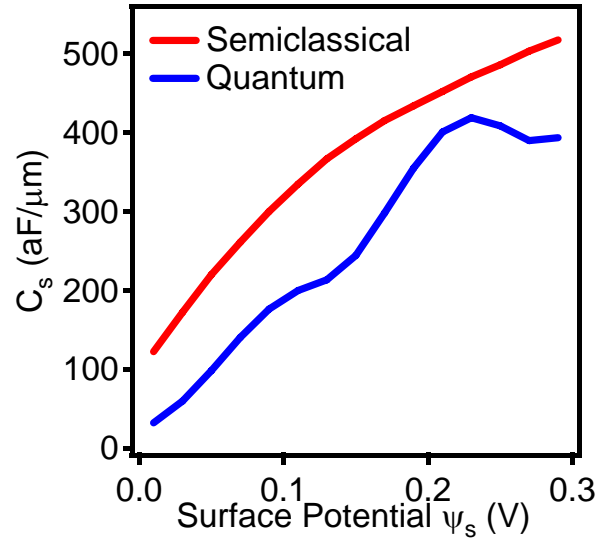


Figure S4. Comparison of semiclassical and quantum semiconductor capacitance as a function of the surface potential for a 20 nm InAs NW at $T=298$ K.

The semiconductor capacitance as a function of the surface potential for a 20 nm InAs NW at $T=298$ K for both the semiclassical simulation and for the quantum simulation is shown in Figure S4. The two peaks in the quantum simulation results are due to the two lowest subbands, with the peaks broadened by the non-uniform potential across the NW cross section and thermal effects at room temperature. When quantum effects are taken into consideration by self-consistently solving the Poisson and Schrödinger equations in the quantum simulation, it is found that quantum effects decrease the semiconductor capacitance by shifting the centroid of the charge away from the NW surface. The quantum effect is expected to slightly increase the threshold voltage due to the quantum confinement energy of the lowest subband. The effect on the total gate capacitance in accumulation region is relatively small however, since the gate oxide thickness is much larger than the NW radius (~ 3 to $7\times$ larger). The gate capacitance is the serial combination of the gate oxide capacitance and the semiconductor capacitance, and the smaller one dominates the total gate capacitance.

The effective electron mobility of InAs NWs

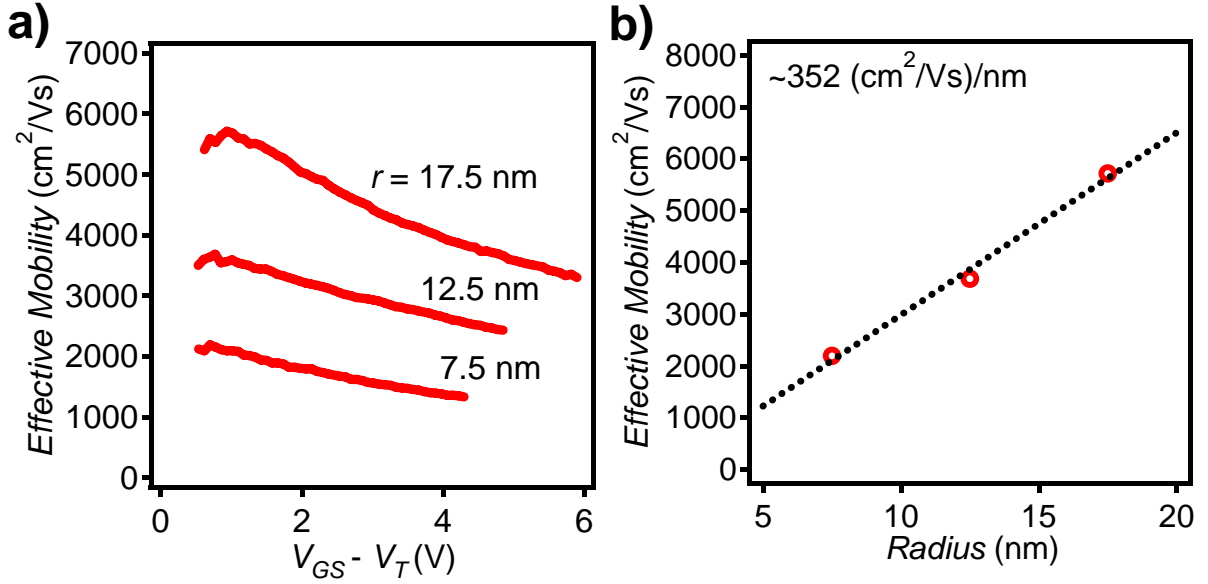


Figure S5. (a) The effective mobility deduced for the devices shown in Figs. 2a and 5a. (b) Peak effective mobility as a function of NW radius for the three devices shown in (a).

The effective mobility was deduced from the I_{DS} - V_{GS} characteristics (Fig. 2a) by using,

$$\mu_{n,eff} = g_D \times \frac{L^2}{C_{ox}} \times \frac{1}{(V_{GS} - V_t)}, \text{ where } g_D = \left. \frac{dI_{DS}}{dV_{DS}} \right|_{V_{GS}}. \text{ The threshold voltage } V_t \text{ is extrapolated}$$

from the I_{DS} - V_{GS} characteristics. For a constant V_{DS} in the linear regime (i.e., $V_{DS}=0.1$ V), g_D is

simply $\frac{I_{DS}}{V_{DS}}$, therefore, the effective mobility can be easily extracted for each gate voltage as

shown in (a). It can be seen that the effective mobility at first increases with the vertical electric

field due to a decrease in the Coulombic scattering, but then decreases for large vertical fields

due to the enhanced surface scattering and contact resistance associated with the Schottky

barriers to the higher subbands. It should be noted that the above analytical expression is not

accurate for $V_{GS}-V_t < 0.5$, therefore, only the effective mobility for the larger $V_{GS}-V_t$ is shown. The

C_{ox} values used to calculate the effective and field-effect mobilities were taken from a fit line of

the experimental data. However, since there is a small difference (~10-15%) between the oxide thicknesses of the *C-V* test structures and the FETs, a ~10-15% uncertainty in the extracted mobility values may be expected.

References

ⁱ Streetman, B. G.; Banerjee, S. K. *Solid State Electronic Devices*, 6th Edition. Prentice Hall, **2006**.